2-1-2020

Hippocampal subfields revealed through unfolding and unsupervised clustering of laminar and morphological features in 3D BigBrain

J. DeKraker
The University of Western Ontario

J. C. Lau
Robarts Research Institute

K. M. Ferko
The University of Western Ontario

A. R. Khan
The University of Western Ontario

S. Köhler
The University of Western Ontario, stefank@uwo.ca

NeuroImage 206 (2020) 116328

Contents lists available at ScienceDirect

NeuroImage

journal homepage: www.elsevier.com/locate/neuroimage

Hippocampal subfields revealed through unfolding and unsupervised clustering of laminar and morphological features in 3D BigBrain

J. DeKraker [a,b,*], J.C. Lau [b,c,d], K.M. Ferko [a,b], A.R. Khan [a,b,c,e,1], S. Köhler [a,f,1]

[a] Brain and Mind Institute, University of Western Ontario, Canada
[b] Robarts Research Institute, Schulich School of Medicine and Dentistry, University of Western Ontario, Canada
[c] School of Biomedical Engineering, University of Western Ontario, Canada
[d] Dept Clinical Neurological Sciences, Division of Neurosurgery, University of Western Ontario, Canada
[e] Dept Medical Biophysics, University of Western Ontario, Canada
[f] Dept Psychology, University of Western Ontario, Canada

ARTICLE INFO

Keywords:
Hippocampus
Subfields
Histology
Cortical folding
Cortical unfolding
Morphology

ABSTRACT

The internal structure of the human hippocampus is challenging to map using histology or neuroimaging due to its complex archicortical folding. Here, we aimed to overcome this challenge using a unique combination of three methods. First, we leveraged a histological dataset with unprecedented 3D coverage, BigBrain. Second, we imposed a computational unfolding framework that respects the topological continuity of hippocampal subfields, which are traditionally defined by laminar composition. Third, we adapted neocortical parcellation techniques to map the hippocampus with respect to not only laminar but also morphological features. Unsupervised clustering of these features revealed subdivisions that closely resemble gold standard manual subfield segmentations. Critically, we also show that morphological features alone are sufficient to derive most hippocampal subfield boundaries. Moreover, some features showed differences within subfields along the hippocampal longitudinal axis. Our findings highlight new characteristics of internal hippocampal structure, and offer new avenues for its characterization with in-vivo neuroimaging.

1. Introduction

The hippocampus is one of the most heavily investigated brain structures in neuroscience. Much research in recent years has focused on questions about its subdivisions, guided by the idea that different regions within the hippocampus may perform different functions and may also be differentially prone to disease (Small et al., 2011). These developments pose central questions as to how to characterize subdivisions in anatomical terms. Traditionally, most proposed subdivisions have relied on histology and cytoarchitecture, leading to the notion of distinct hippocampal subfields that typically include the subicular complex, Cornu Ammonis 1 to 4, and the dentate gyrus (Duvernoy et al., 2013). More recently, increasing interest has also emerged concerning graded differences along the anterior-posterior axis based on subfield composition and connectivity (Strange et al., 2014; Poppenk et al., 2013; Plachti et al., 2019). An organizational principle that shapes these dimensions, i.e., subfields and anterior-posterior differences, is the complex topology within the hippocampus that results from folding during its ontological development (Duvernoy et al., 2013; DeKraker et al., 2018). This principle has received only limited investigation to date but requires careful consideration in any effort to characterize the internal architecture of the hippocampus. The current paper aims to investigate the relationship between hippocampal morphology and laminar cytoarchitecture under a topological framework in humans. In other words, the goal is to examine laminar and morphological (ie. non-laminar) features, such as cortical thickness or curvature, within a framework that explicitly honours 3D continuity across 2D images. In order to pursue this goal, we took advantage of the unique and powerful "BigBrain" dataset that provides continuous histological sampling with full 3D coverage (Amunts et al., 2013). A particular promise of this approach lies in its applicability to in-vivo Magnetic Resonance Imaging (MRI).

While commonly used MRI measures do not allow for cytoarchitectural characterization, MR-based protocols have been developed to indirectly infer the locations of hippocampal subfields in humans based

* Corresponding author. Robarts Research Institute, Western University, 1151 Richmond St. N, London, Ontario, N6A 5B7, Canada.
E-mail address: jdekrake@uwo.ca (J. DeKraker).
[1] co-senior authorship.

https://doi.org/10.1016/j.neuroimage.2019.116328
Received 5 July 2019; Received in revised form 29 October 2019; Accepted 30 October 2019
Available online 1 November 2019

either on manually delineated landmarks or corresponding probabilistic atlases that are informed by histological reference material (Yushkevich et al., 2015a, 2015b; Iglesias et al., 2015). However, traditional histological references can be problematic for several reasons. First, they often contain only select coronal slices taken from regions where folding is the simplest, most frequently from the hippocampal body, with the notable exception of (Ding and Van Hoesen, 2015) who focus greater attention on the hippocampal head than most other investigations. Second, even in the hippocampal body slices are taken sparsely, limiting the amount of contextual features that can be gathered from neighbouring slices or other planes of view. Third, histological preparation often deforms the tissue of interest relative to its in-vivo state, which is a problem for MRI co-registration unless the histological sample is also imaged prior to histological preparation. Finally, even among neuroanatomists there is some disagreement as to exactly which labels, stains, and histological features should be used for defining hippocampal subfields (Wisse et al., 2017). Some previous studies have made use of ex-vivo MRI to aid in the translation of histology to MRI (Iglesias et al., 2015; Yushkevich et al., 2009) in an effort to mitigate some of these issues. However, even with such an approach, inter-individual differences in hippocampal morphology can impose limitations for inferring subfields or other structural features, when hippocampal topology is not considered.

It is well established that the human hippocampus is a folded component of archicortex that is continuous with the neocortex (Duvernoy et al., 2013; Nieuwenhuys et al., 2013). The hippocampal folds include wrapping around its innermost region - the dentate gyrus, as well as anterior-posterior folding that is sometimes referred to as dentation, digitation, or gyrification. The gyrification seen in the hippocampus is morphologically similar to gyrification in the neocortex (although not necessarily based on the same ontogeny). It has been shown to vary considerably between individuals (DeKraker et al., 2018; Chang et al., 2018) and can be affected by age (Cai et al., 2019) or disease, such as temporal-lobe epilepsy (Blümcke et al., 2013). This folding is an important aspect of understanding the internal structure of the hippocampus, and for appreciation of the continuity of subfields, particularly in its anterior portion that includes the uncus (Ding and Van Hoesen, 2015). Topological analyses can provide a framework for extracting these continuities, for example through unfolding (DeKraker et al., 2018), and offer the basis for laminar and further morphological characterization of complete hippocampal structure in 3D, including subject-specific gyrification.

The dataset made publicly available by BigBrain (Amunts et al., 2013) provides a unique opportunity to conduct topological analyses of histology data in 3D, and to examine topological measures in unfolded tissue. This dataset consists of 3D histology, digitally reconstructed from images of serially sectioned and stained cadaveric brain tissue. In the current project, we used reconstructed blocks of the left and right hippocampi (40μm isotropic) from BigBrain to identify topologically-derived laminar and morphological features under our hippocampal unfolding framework. To characterize laminae, we focused on 10 computationally derived features describing the distributions of neurons (Amunts et al., 1999), which were also recently used to characterize the neocortex in BigBrain (Wagstyl et al., 2018; Wagstyl et al., *bioRxiv*). Morphological features were also computationally derived and included thickness, curvature, inner and outer surface textures, as well as gyrification. We then compared these morphological and laminar features to classic descriptions of subfields and examined variations along the anterior-posterior hippocampal axis. We anticipated that the features examined would differ substantially between subfields. Therefore, we also tested whether it might even be possible to obtain successful subfield segmentation with an unsupervised feature-based approach. This type of approach is desirable for is objectivity, which could help resolve differences among neuroimagers and histologists on subfields definitions. It also allowed us to examine which subsets of features are sufficient to derive clusters resembling gold standard hippocampal subfields. For this purpose, we contrasted the contributions of laminar and morphological features, given that laminar features are used most prominently in histology (see Duvernoy et al., 2013; Nieuwenhuys et al., 2013) but morphological features, such as thickness, are more readily available in high-resolution structural MRI (e.g. DeKraker et al., 2018).

2. Materials and Methods

The backbone of our analyses was to impose a topological unfolding framework to manual hippocampal traces, a method that we previously developed for 7T MRI (DeKraker et al., 2018). We then extracted various morphological features of hippocampal structure from the left and right BigBrain hippocampi. We computed laminar features based on the work of (Amunts et al., 1999) and modelled as in (Waehnert et al., 2014). We then performed unsupervised, data-driven clustering of these features and compared resulting clusters to manually segmented hippocampal subfields. Finally, we examined differences in hippocampal structure along its longitudinal (i.e., anterior-posterior) axis.

2.1. Materials

Histological data used in this study came from the BigBrain dataset, which consists of serially sectioned and stained brain tissue that was then reconstructed in 3D. Specifically, in the present study we used bilateral 40 μm^3 resolution hippocampal blocks (ftp://bigbrain.loris.ca/BigBrainRelease.2015/3D_ROIs/Hippocampus/) in addition to serial section images at 20 μm^2 resolution (ftp://bigbrain.loris.ca/BigBrainRelease.2015/2D_Final_Sections/Coronal/Png/Full_Resolution/) (Amunts et al., 2013). BigBrain preparation involved silver staining, which selectively targets cell bodies, providing a contrast that is different from, but conceptually similar to, Grey Level Index (Wagstyl et al., 2018; Schleicher et al., 1999). Because of the large file sizes, tracing and application of our unfolding framework were performed on down-sampled images (80μm isotropic) before upsampling by nearest-neighbour interpolation in the case of labelmaps, and linear interpolation in the case of unfolding solutions.

2.2. Manual tracing

Detailed histological tracing was performed for each hippocampus by a combination of manual tracing and the user-guided computational tools in ITK-SNAP 3.6 (Yushkevich et al., 2006). ITK-SNAP is primarily used for manual tracing using a 2D or 3D paintbrush, but it additionally contains some semi-automated tools that were used at the manual tracer's discretion, including morphological operations such as dilation and erosion. Since these tools rely so closely on the supervision of the tracer, we will refer to the use of these tools as a manual process throughout this manuscript. All traces were performed in native space, using all three view planes. A general label for hippocampal grey matter (subiculum and CA1-4) was manually traced first, and this tissue was later manually divided into subfields. Only the laminae which contained stained neuronal cell bodies - stratum pyramidale, oriens, and lucidum - were traced (Fig. 1). Stratum radiatum lacunosum and moleculare (SRLM) and the alveus were not traced even though they are sometimes considered laminae of the archicortex containing dendrites and axons of pyramidal cells (Duvernoy et al., 2013); they were not stained by this contrast (although note that some of these strata contain interneurons - see Supplementary Materials section A for discussion).

Subfield segmentation (i.e. the division of archicortical grey matter into distinct subfields) was performed in 3D by rater Kayla Ferko (KF) according to the criteria outlined by (Ding and Van Hoesen, 2015). This work provides a detailed and instructive guide to segmenting all subfields of the hippocampus, including the hippocampal head with multiple samples with varied folding structure. One limitation of our segmentations is that Ding et al.'s protocol includes the use of both neuronal body and myelin stains, whereas no myelin stain is available in the BigBrain dataset. To take full advantage of the histological features available in

BigBrain and make use of the highest resolution available, original 20 μm images were also consulted every 2 mm. In other words, subfield borders on the 80 μm 3D hippocampus were manually compared to borders on 20 μm 2D images and, where necessary, the 80 μm borders were updated to best match 20 μm images. These segmentations included the subiculum and CA1-4, but did not differentiate the regions within the subicular complex due to lack of resolution and since no myelin staining was available. Subfields were traced through the entire length of the hippocampus including the uncus and vertical component of the uncus, in which (Ding and Van Hoesen, 2015) describe modified versions of the same subfields. Because the vertical component of the uncus is very thin, its subfields were not easily discriminable. As a consequence, they were partially inferred from neighbouring regions of the hippocampus. Smoothing of the final traces was then performed by label-specific dilation (e.g. dilating subiculum 4 voxels over CA1; then dilating CA1 8 voxels over subiculum; then dilating subiculum 4 voxels over CA1 again, while always ensuring dilation was balanced in both directions). This was performed for all subfields in the order CA4-CA3-CA2-CA1-subiculum, ensuring that subfield borders followed smooth transitions from slice to slice.

Structures surrounding the hippocampus were traced only in the regions that border the hippocampus. These labels included medial-temporal lobe neocortex (MTLc) (entorhinal and parahippocampal regions), hippocampal-amygdalar transition area (HATA), and indusium griseum (ind. gris.). HATA borders were clearly discriminable from archicortex by a marked change in density and physical separation from archicortical neurons. Ind. gris. and MTLc borders were less clear, and so they were demarcated using the heuristics used in previous work in MRI (for example, the MTLc-subiculum boundary is defined at the supermedial edge of the white matter in the parahippocampal gyrus. See

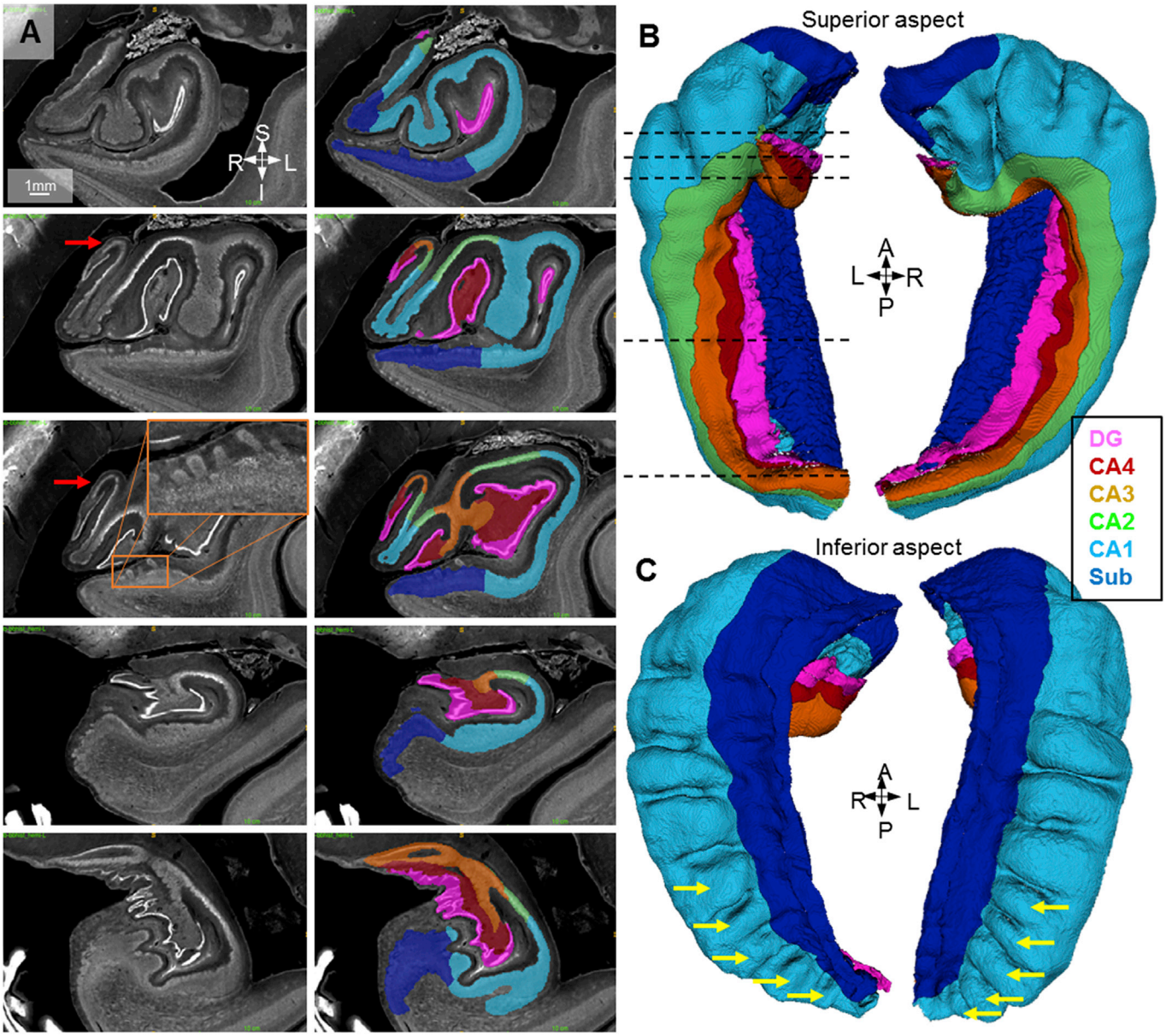

Fig. 1. Manual traces of hippocampal archicortex and segmentation into subfields. A) shows coronal slices through the left hippocampal head (rows 1–3) body (row 4) and tail (row 5), with manual segmentations overlaid in the images to the right. Images were taken from coronal slices 716, 632, 590, 376, and 230 of the 40 μm native space left hippocampal block. B) shows 3D models of each hippocampus as seen from their superior aspect, with the inferior aspect shown in C). Dotted lines in B) indicate approximate locations of each coronal slice shown in A). SRLM, vestigial hippocampal sulcus, alveus, and fimbria were excluded from all labels. Red arrows indicate anterior folding in the vertical component of the uncus, the orange inset in the third row highlights 'islands' of neuronal cell bodies in the subicular stratum lacunosum, and yellow arrows indicate gyrifications in the posterior body and tail of the hippocampus.

(DeKraker et al., 2018) for further details). See Supplementary Materials section A for further discussion of these structures.

2.3. Topological unfolding framework

In previous work (DeKraker et al., 2018), we imposed a topological unfolding framework on the hippocampus by solving Laplace's equation over the domain of the hippocampus under multiple sets of boundary conditions: anterior-posterior, proximal-distal, and laminar. The anterior-posterior and proximal-distal solutions can then be used to index regions of the hippocampus in 2D according to its topology, irrespective of inter-individual differences in gyrifications, rotation, curvature, size, orientation, or position of the hippocampus. This provides implicit registration between hippocampi despite inherently different morphologies. Data can be transformed between native and unfolded space bidirectionally using interpolation. We applied this same approach to BigBrain hippocampal traces (see Fig. 2 for illustration). However, note that several minor improvements were made to this code which are detailed in Supplementary Materials section B. Most notably, instead of binning maps into 100×100 pixels, they were instead derived from a midsurface mesh consisting of 512×256 vertices, with data being sampled from all features by nearest neighbour. The dentate gyrus (DG) was not included in this unfolding. Although it was easily distinguishable from other subfields by its very high cell density, it is topologically disconnected from the rest of the archicortex, and therefore would be out-of-plane (i.e. perpendicular) to our unfolded space (see Fig. 1 for visualization).

Waehnert et al. noted that neocortical laminae are displaced due to curvature in gyri and sulci, and they propose an 'Equivolume' model that captures this feature better than a Laplacian (or equipotential) solution (Waehnert et al., 2014). Their model is motivated by the observation that a given lamina, for example near the pial surface, will stretch at the apex of a gyrus and compress at the depth of a sulcus, causing it to become thinner and thicker in these respective regions, and vice versa for laminae at the white matter surface. Thus, we also included an alternative laminar indexing system using the Equivolume model solution obtained from Nighres (Landman et al., 2013). Again, this was performed on the downsampled (80μm) traces before upsampling as described above. The resulting model had fewer gyrification-related artifacts in laminar profiles and was used for all subsequent laminar analyses. However, some other artifacts were observed under this model solution, likely as a result of the rough texture of the subiculum surface (see Supplementary Materials section C for details). These laminar profiles were extracted for each unfolded point ($512 \times 256 \times 16$ points, or vertices) at the corresponding nearest neighbour (full resolution) native space voxel.

2.4. Morphological feature extraction

Each morphological feature is illustrated in the top left panel of Fig. 3. Thickness estimates were obtained across the unfolded space of the hippocampus as in previous work, that is, by generating and measuring streamlines in 3D across the laminar Laplacian solution obtained from our topological unfolding framework. Curvature estimates were obtained by generating a mid-surface along the hippocampus with the vertices being interpolated xyz coordinates from each unfolded point at a laminar distance of 0.5, which is the midpoint between the inner and outer surface. Smoothing of face normals was applied, and mean curvature was then estimated at each vertex (see Supplementary Materials section B for details). The inner (i.e. adjacent to the SRLM; continuous with the neocortical pial surface) and outer (i.e. adjacent to the alveus, continuous with the neocortical white matter surface) surfaces of the hippocampus were rougher than their mid-surface counterpart due to the presence of other features, such as subicular 'islands' of cell bodies shown in Fig. 1. Thus, we additionally computed curvatures of these surfaces after smoothing as described above. Gyrification is typically defined as a ratio outer surface area, for example that of a brain mask over gyrified surface area, in this example including sulcal area (Larsen et al., 2006). Since the hippocampus is an open-ended cortical surface it does not map easily to an outer surface area or to a sphere as in the neocortex, and so our unfolding framework instead maps it to a rectangle. We thus defined gyrification as a ratio of native space surface area over unfolded surface area at each unfolded point.

2.5. Laminar feature extraction

We extracted laminar profiles along the Equivolume laminar solution described above, and then summarized these profiles using the same 10 features consistently used by (Amunts et al., 1999; Wagstyl et al., 2018).

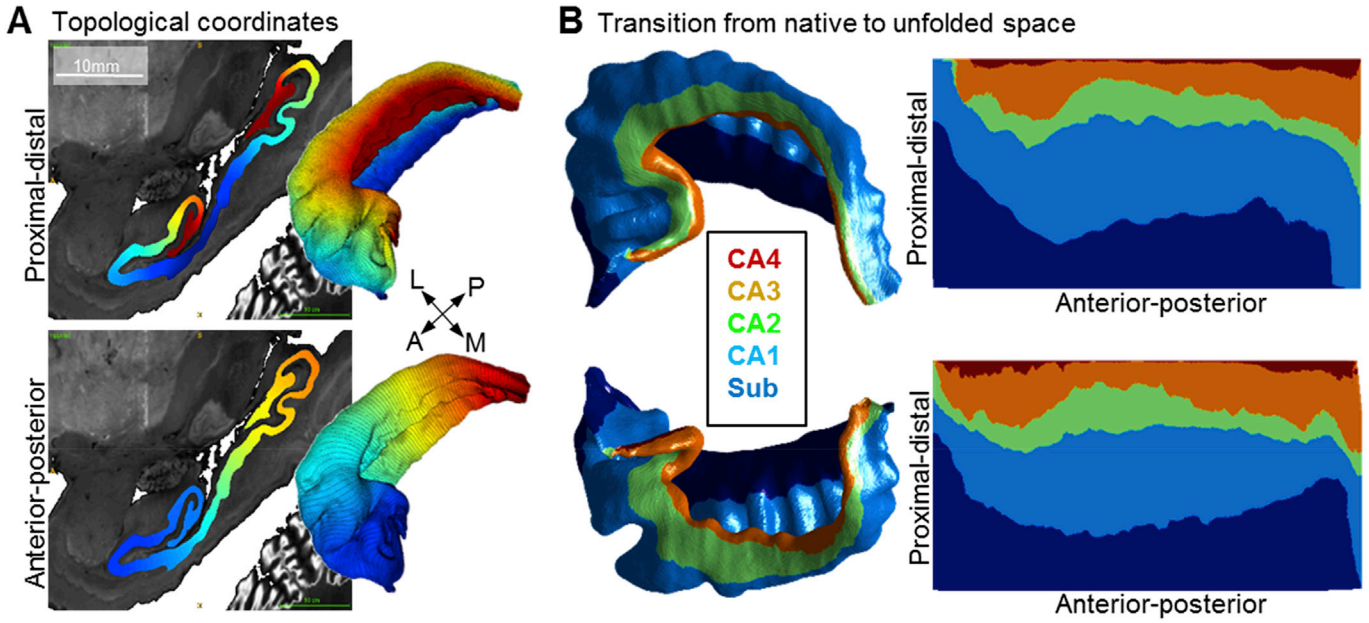

Fig. 2. Topological unfolding framework in BigBrain with hippocampal subfields. A) Sagittal slice and 3D models of the Laplacian solutions (proximal-distal and anterior-posterior) for the right hippocampus. Image was taken from sagittal slice 514 of the 40 μm native space left hippocampal block. B) Mid-surface topological models of the left and right hippocampi in native and unfolded space.

Briefly, this involved sampling staining intensities (y) along a laminar profile through the cortex, and calculating the mean (Mean(y)). This intensity profile was then treated as a distribution (x), and the mean (Mean(x)) and first 3 moments (SD(x), Skew(x), and Kurt(x)) were calculated. The absolute value of the derivative (Abs.Deriv) of the profile was then calculated (y→y.d), and the same measures (e.g. Mean(y.d), Mean(x.d), etc) were obtained. These methods are illustrated with corresponding terminology at the top of Fig. 3.

There were several methods developed for 3D MRI, which we were able to incorporate into this analysis, with resulting differences when compared with the analyses performed by (Amunts et al., 1999). Firstly, we sampled laminar profiles under the 3D Equivolume model that minimizes distortions in laminae due to curvature (as discussed above). Secondly, our laminar sampling was not as dense because of the reduced resolution available in the current data, and the fact that the laminae of the archicortex are generally thinner than those of the neocortex. Lastly, we included only laminae containing neuronal cell bodies (as discussed above). Further details on these differences between our methods and those of (Amunts et al., 1999) can be found in Supplementary Materials section B.

2.6. Unsupervised clustering

In order to cluster visually-homologous regions of the feature maps into segments, we applied a scale-space representation employing image pyramids. That is, for each of the selected features, we smoothed the data in unfolded space with a Gaussian kernel and a Laplacian of Gaussian kernel of sizes sigma = 0.16, 0.32, 0.64, 1.28, and 2.56 mm in order to capture features at various spatial scales. Because unfolded space does not necessarily have correspondence to real-world size, we reparameterized our unfolded space according to real-world distances between points prior to smoothing, and then returned the resulting smoothed feature maps to the original unfolded space parameterization. See Supplementary Materials section E for details and visualization of this

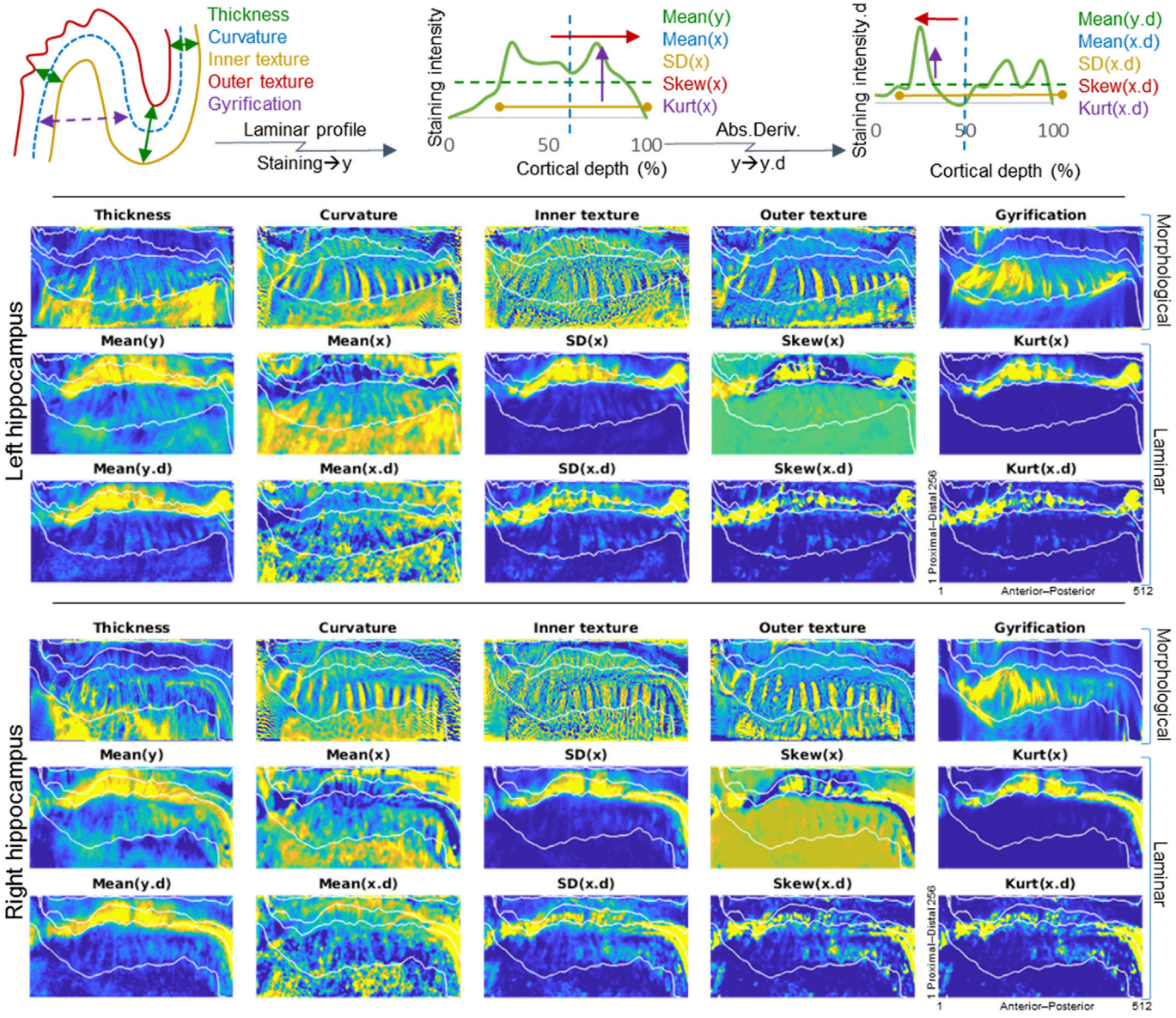

Fig. 3. Characterization of the hippocampus using morphological and laminar features. The top diagrams illustrate how each feature is derived (see Materials and Methods section for details). Top left shows an example segment of cortex, while the top centre and top right show an example laminar profile and its absolute derivative (Abs.Deriv), respectively (Amunts et al., 1999). Heat maps below show the z-scored values of each feature across the unfolded hippocampus in the left and right hemispheres, with the same colour scaling in both hemispheres. Overlaid in white are manually defined subfield borders, the top edge being the border with the DG which is out-of-plane.

reparameterization. This multi-scale smoothing is meant to reduce noise in the data, but also to provide some spatial regularization of features, ensuring that resulting clusters will not be distributed in only small patches. The anterior 10% and posterior 10% of each feature were discarded due to high noise.

All morphological and laminar features from the left and right hippocampi were then reshaped into single vectors, z-scored, and entered into a principal components analysis (PCA). K-means clustering was then computed on the first 8 components, which explained >1% variance each, with a fixed number of output clusters of k = 5 (since manual segmentations contained 5 subfield labels). PCA followed by K-means clustering was ideal for this type of analysis for several reasons: 1) Co-linearity among features can be clearly assessed using PCA prior to k-means clustering; 2) Clusters were expected to be of comparable sizes, which k-means is biased towards; and 3) The number of clusters is known a-priori. Clusters were then assigned subfield labels based on highest overlap. Dice overlap scores were calculated (Dice, 1945; Sørensen, 1948) in unfolded space for each subfield (i.e. disregarding thickness), excluding the 10% anterior and posterior edges that were removed due to high noise. Dice was also calculated in native space, which is shown in Supplementary Materials section D. In this case, however, clusters had to be extrapolated over the 10% anterior and posterior regions leading to lower total overlap scores. We also explored clustering under k = [2,4,8, 16,32], and performed alternative clustering methods, in order to determine the consistency of subfields and sensitivity to further subdivisions in the data, with results described in Supplementary Materials section D. In brief, these results support the validity of the clustering methods we employed, and show that when other methods are used, cluster boundaries occur at locations similar to those reported in the main body of this article. PCA variance explained per component, component loadings and visualization of the first 8 components can be viewed in Fig. 5, along with the correlations between all features.

In order to determine whether subfield clustering could be derived using only laminar features or only morphological features alone, we repeated the above process for the subsets of morphological and laminar features separately. We used the same '>1% variance explained' threshold to remove PCA 'noise' components, which resulted in 5 components in the laminar feature clustering, and 3 components in the morphological feature clustering. Morphological features of inner and outer surface textures were excluded since they capture subicular 'islands' of cell bodies in stratum lacunosum, which could be considered a laminar feature. This exclusion was also based on the limited value of these two features for any MRI assessment.

2.7. Anterior-posterior variation

One hypothesis that we had based on prior literature was that there may be anterior-posterior differences in some aspects of hippocampal structure (Strange et al., 2014; Poppenk et al., 2013; Plachti et al., 2019). We thus plotted select features of interest across the anterior-posterior axis within each subfield. All features can be seen in a Supplementary Materials section A, where we additionally fit linear trends to the data to determine whether anterior-posterior gradients were present in any subfield. In Fig. 6 we display the features mean neuronal density (Mean(y)), thickness, and gyrification that most clearly differed between subfields and are of immediate interest in MRI.

3. Results

3.1. Manual tracing

Fig. 1 shows BigBrain coronal slices alongside manually segmented subfields in the head, body, and tail of the hippocampus, as well as corresponding 3D models. Several features were detected in tracings of the hippocampus in BigBrain that were not detected in previous in-vivo MRI work that we know of. Clusters of pyramidal cells or 'islands' can be seen on the inner surface of the subiculum (stratum lacunosum), which have been observed in histology throughout the presubiculum (Duvernoy et al., 2013; Ding and Van Hoesen, 2015). A medial and anterior fold along the vertical component of the uncus, approximately 0.3 mm thick and up to 3.6 mm in length, was observed, as described in (Duvernoy et al., 2013; Ding and Van Hoesen, 2015). Finally, numerous gyrifications throughout the posterior body and tail of the hippocampus were observed, which have previously also been observed using MRI in (Chang et al., 2018), although not to the extent seen here. This was most prominent in CA1, but was also present in the DG and in CA4, which followed the same gyrification scheme as CA1. Models of the dentate gyrus alone and additional anatomical notes can be found in Supplementary Materials section A. Total volumes of each subfield can be seen in Table 1. Note that these volumes are smaller than what is typically reported in MRI. This may be due to our exclusion of alveus and SRLM laminae, which can be hard to differentiate from partial voluming in MRI, but may also be influenced by tissue shrinkage during histological processing. Furthermore, the issue of partial voluming in MRI may be exacerbated by the presence of gyrifications, which appeared more prominent in the right BigBrain hippocampus. These gyri are discussed in greater detail in Supplementary Materials Section A.

3.2. Topological unfolding

Fig. 2A shows the proximal-distal and anterior-posterior Laplacian solutions that make up the two axes of our topological unfolded space. The dentate gyrus (DG) was not unfolded. Although it was easily distinguishable from other subfields by its very high cell density it is topologically disconnected from the rest of the archicortex, and therefore would be out-of-plane (i.e. perpendicular) to our unfolded space (see Fig. 1 for visualization). Fig. 2B shows a mid-surface mesh of the hippocampus, coloured according to manually segmented subfields as in Fig. 1. This surface was then mapped to 2D unfolded space according to the anterior-posterior and proximal-distal Laplace solutions. In unfolded space, subfields are relatively constant from anterior to posterior, with subiculum being proportionally larger in the very anterior and smaller in the very posterior extent. However, these differences may be artifacts of manual segmentation since these regions are very small in native space. This unfolding is illustrated in our online video (created through linear interpolation of all points between native and unfolded space).

3.3. Characterization of the hippocampus in unfolded space

Fig. 3 shows a full characterization of the left and right BigBrain hippocampi with respect to the 5 morphological and 10 laminar features. These features are illustrated at the top of the figure, but additional details can be found in the Materials and Methods section. As in related work (Duvernoy et al., 2013; DeKraker et al., 2018), thickness was highest in the subiculum and CA4 and lowest in CA2. Curvature was generally high in subiculum, which reflects its outward curling away from the rest of the hippocampus. In CA1, vertical bands of positive and negative values can be seen that correspond to the hippocampal gyrifications displayed in Fig. 1. This region is also highlighted by our gyrification measure, which differs from curvature in that it does not vary by direction. Inner surface texture shows an almost honeycomb texture that

Table 1
Volumes of each manually defined subfield (mm^3).

	Left	Right
Sub	345.9	282.5
CA1	574.0	534.0
CA2	46.6	40.6
CA3	66.9	54.4
CA4	109.0	107.4
DG	140.1	131.1

is most prominent in the subiculum, where subicular 'islands' of neurons are found in stratum lacunosum (Duvernoy et al., 2013). Outer surface texture appears smoother, and more closely resembles the mid-surface curvature measure. Note that the surface textures measures differ from the curvature measure only in that they capture very local details. Thus, they may not be available in lower resolution data. By contrast, features such as thickness and gyrification may be especially of interest in translation of this work to MRI, particularly because they show such clear distinction between subfields.

Of the laminar features computed here, Mean(y) was highest in region CA2, which also agrees with the high neuronal densities observed in this region (Duvernoy et al., 2013). Mean(x) showed almost the inverse pattern, with high values in all regions except CA2. This means that the distribution of neurons was shifted towards the inner surface in CA2. SD(x) was highest in CA2, indicating a wide distribution of neurons relative to the thickness of that tissue. This was counter-intuitive since in native space CA2 appears to have a tight distribution of neurons; however, relative to its small thickness the distribution is wide. The remaining 8 laminar features become more complex and quite similar to Mean(y), Mean(x) or SD(x). Thus, some of these features may be redundant. We nevertheless included them for consistency with previous work in the neocortex (Amunts et al., 1999). Although we did not perform any systematic comparison, there is visibly very high consistency in all features between the left and right hippocampus, particularly with respect to the subfields.

3.4. Unsupervised identification of hippocampal subfields using combination of morphological and laminar features

By visual inspection, many of the features in Fig. 3 show a clear distinction between the different manually defined subfields. Therefore, we sought to determine whether a combination of these features could be used to derive some or all of the subfield boundaries between subiculum and CA1 to CA4 computationally, using PCA followed by k-means clustering (see Materials and Methods for details). In this endeavor we also examined whether morphological or laminar features in isolation would be sufficient to allow for successful clustering, i.e. to derive clusters that closely resemble gold standard hippocampal subfields. For consideration of morphological features, we excluded surface textures given that they include subicular 'islands', which arguably also qualify as laminar features (see Supplementary Materials section D, and Ding and Van Hoesen, 2015; Ding, 2013 for further discussion). Fig. 4 shows the results of unsupervised clustering of the combined feature sets, laminar features only, and morphological features only. We compared clusters to their closest corresponding manually defined subfield (gold standard) using Dice overlap scores in Table 2. When all features were combined in this analysis, good (0.7) to very good (0.8+) overlap was found for most subfields. Specifically, subfields subiculum, CA1, as well as combined CA2 and CA3 showed overlap with gold standard segmentations. Manually defined region CA2 had two clusters that overlapped with it (orange and green in Fig. 4). The green cluster corresponded to the most dense regions of CA2 (e.g. where Mean(y) and SD(x) were high), and several other laminar features echoed this pattern. The fact that multiple features showed this pattern may have contributed to the generation of two clusters in CA2. In other words, the variance within CA2 may have been amplified by the presence of redundant features. Using a combination of labels CA2 and CA3, as is often done in MRI segmentation protocols (Yushkevich et al., 2015a), increased the Dice overlap scores as expected. We note that subfield CA4 did not emerge as a unique cluster and was instead included in the same cluster as CA1 or CA3. This remained true even when the number of clusters (k) was increased up to $k = 16$ (Supplementary Materials section D). Overlap of CA4 with CA3 is to be expected given their topological closeness, but overlap with CA1 is more surprising. One possible explanation is that despite their topological separation, both of these regions were thicker, had higher gyrification, and contained a lower density of neurons than CA2 and CA3 (see Fig. 3; CA4 is at the very top of each map). Relabeling clusters 1 and 2 (when they were present) past a proximal-distal distance of 200 allowed us to force a separation based on its break in continuity (i.e., separation in unfolded space, see Table 2). It should be noted that this latter approach is not purely data-driven and only offers a heuristic that is built on a-priori knowledge. Finally, the current analyses did not reveal any evidence for the subregions of the subicular complex as described by (Ding, 2013). This is not surprising because BigBrain only contains a single contrast (neuronal cell bodies); other contrasts (particularly myelin) or even immunochemical profiles are typically used to detect these subregions (Ding and Van Hoesen, 2015; Ding, 2013). Converging evidence was obtained for these results using different numbers of clusters, k, in k-means clustering, and using a different clustering algorithm, i.e., hierarchical clustering (see Supplementary Materials section D).

3.5. Unsupervised identification of hippocampal subfields using morphological or laminar features in isolation

We next asked whether subsets of features (i.e. morphological features alone or laminar features alone) could be used to derive hippocampal subfield borders. Laminar features alone were able to capture most boundaries with good accuracy, with the exceptions of CA1, CA2, and CA3 which had Dice scores below 0.7. (Fig. 4; Table 2). Again, combining CA2 and CA3 lead to good (0.7+) agreement with manually defined gold standard segmentations. CA1 was less well defined using only laminar features, and indeed there is some disagreement over the exact border between subiculum and CA1 in the histological literature (some disagreement may depend on the inclusion of prosubiculum as its own region or simply a transition zone; see (Wisse et al., 2017). Morphological features alone revealed two clusters within subiculum and two within CA1, and did not differentiate between CA2 and CA3 at all. Clustering using these features also highlighted boundaries surrounding CA4, but CA4 did not contain a unique cluster. Rather, the same clusters that were assigned to CA1 were assigned to CA4, similarly to when all features were included in clustering. However, it is worth noting that when their topological separation is considered visually, CA4 can easily be distinguished from CA1. Overall with the exception of differentiating CA2 from CA3, morphological features were sufficient to delineate hippocampal subfields with very good (0.8 + in most cases) accuracies, at a level similar to clustering based on the combination of all features.

3.6. Relative contributions of individual features to subfield clustering

In order to better understand the inherent structure of the data used in the above k-means clustering of all features, we revisited the PCA that guided clustering and examined various PCA metrics. Fig. 5A shows the total variance explained by each PCA component; only the first 8 components explained >1% of the variance and were included in subsequent analyses. Fig. 5B and D shows a breakdown of the first 8 principal components. The first and most prominent component was most highly correlated with most laminar features, except Mean(x), Skew(x), and Mean(x.d) which showed an anti-correlation. Visualization of this component shows consistently high values in CA2. This makes sense since most laminar features showed uniquely high values in CA2, while Mean(x), Skew(x), and Mean(x.d) contained low values in this region (Fig. 3). Subsequent components explain a decreasing portion of the total variance in the data, but correlate with different input features. Visual inspection of these components shows that some loosely follow the contours of the subfields. For example, component 3 quite clearly alternates high and low between subiculum, CA1, CA2, and CA3. Others, particularly components 5–8, appear to contain little subfield-related variance and may reflect noise captured by the later components. Interestingly, components 2 and 3 appear to show gradual anterior-posterior differences, with higher values in the anterior and lower values in the posterior extent in component 2, and the opposite pattern in component 3.

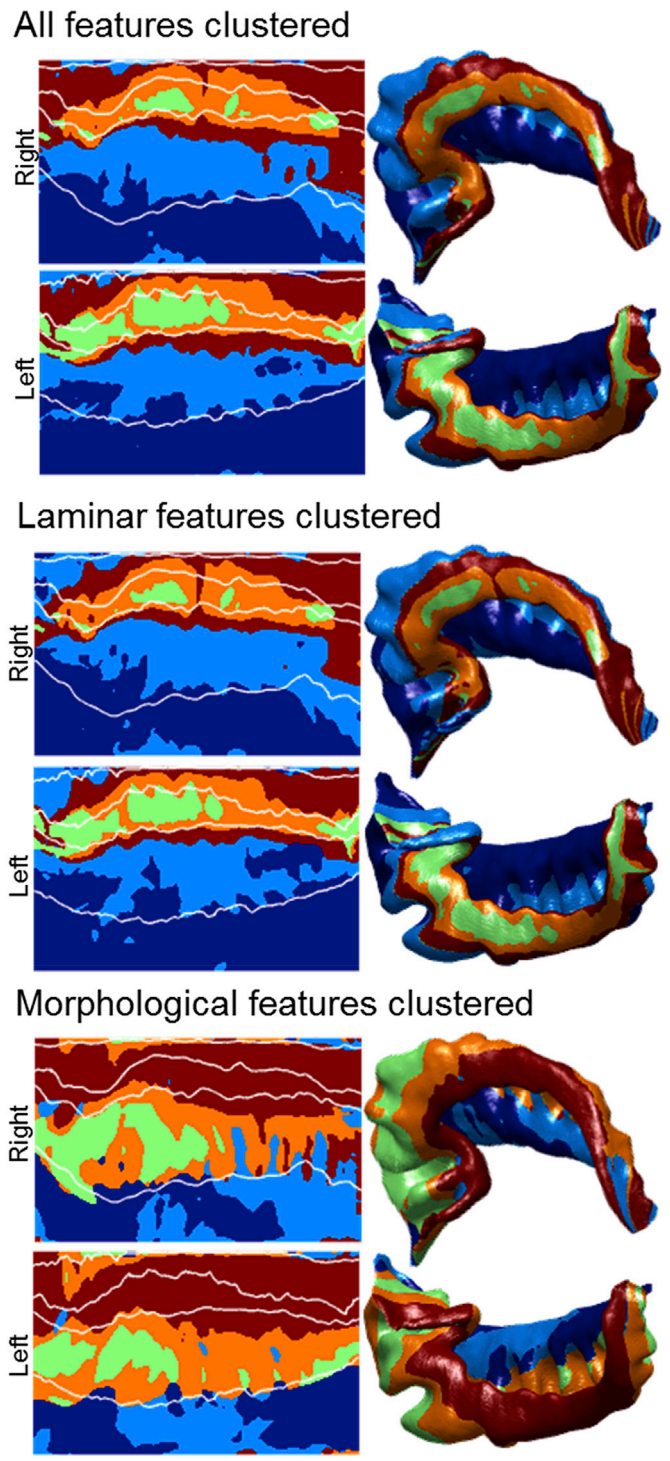

Fig. 4. Unsupervised k-means clustering of features. The left images show k-means clusters in unfolded space at k = 5, with manually defined subfield borders overlaid in white. The right images show the same data in native space, with 10% anterior and posterior edges extrapolated by nearest neighbour. Clustering was completed for the combined set of all features, laminar features only, and morphological features only.

Of the features used in this analysis, some were more correlated with each other than others (Fig. 5C). In particular, all morphological features tended to be correlated with each other. All laminar features tended to be correlated or anti-correlated with each other, with only small correlations between morphological and laminar features. The fact that laminar features tended to be uncorrelated with morphological features is in line with the goal of the Equivolume model (Waehnert et al., 2014), which we applied in order to remove the effects of curvature on laminar displacement. Thus, overall, when modelled in 3D using the appropriate methods, morphological and laminar features represent different levels of structural information about tissue within the hippocampus. One notable exception is that thickness was anti-correlated with many laminar features. This could be due to measurement bias: If thickness were overestimated in manual segmentation, then laminar profiles would be systematically shifted. However, this may also relate to how microstructural differentiation of local tissue features contribute to overall cortical thickness (see Wagstyl et al., 2018 for discussion).

3.7. Structural variation along the longitudinal hippocampal axis

In a final set of analyses, we aimed to explore qualitatively whether subfields would show differences in feature composition along the anterior-posterior axis of the hippocampus. Towards this end we visualized possible trends along the axis in each manually-defined subfield (Fig. 6). We primarily focused on the features gyrification, thickness, and mean neuronal density (Mean(y)), given that these features showed high contrast between different subfields. (Data for all other features are included in Supplementary Materials section A). Note that with this visualization, a high degree of separation can be seen between some subfields, as previously described (see Fig. 3). Thickness and gyrification tended to show lower values at the anterior and posterior extremes, or in the vertical component of the uncus and tail of the hippocampus. This pattern was also observed during manual tracing (Fig. 1). However, in the remainder of the hippocampus, namely the head and body, thickness remained relatively constant in each subfield while gyrification gradually decreased, as observed during manual tracing. This is most notable in CA1 where gyrification is especially prominent (note that in the Supplementary Materials section A, we also report a similar linear decrease in gyrification in CA3, but at a much smaller scale). Neuronal density was notably lower in most subfields in the anterior sections, approximately corresponding to the vertical component of the uncus. Additionally, subfield CA1 and CA4 showed linear increases in density from anterior to posterior (Supplementary Materials section A). Overall, these visualizations suggest that anterior-posterior differences are clearly present in gyrification in CA1, and in density in CA1 and CA4.

4. Discussion

In the present study we show, for the first time, unsupervised clustering of human hippocampal subfields that closely resembles the manually defined gold standard. We additionally show that morphological features alone are sufficient to derive most hippocampal subfield boundaries. Moreover, our findings reveal that some features, most notably gyrification in CA1, showed within-subfield differences along the anterior-posterior hippocampal axis. The current study sheds new light on the relationship between hippocampal topology, morphology, and laminar cytoarchitecture with respect to hippocampal subfields and the anterior-posterior axis.

4.1. Structural characterization of the hippocampus in BigBrain

Manual tracing and 3D modelling of the hippocampus (Fig. 1) at the level of resolution available in BigBrain revealed several features not seen in any 3D atlas that we are aware of. First, medial folding in the posterior end of the vertical component of the uncus was observed, similar to the inward 'curling' of the CA fields around the innermost DG in the rest of the hippocampus. Second, 'islands' of pyramidal neurons were present in stratum lacunosum in the subiculum. Third, gyrifications were present throughout the head, body, and tail of the hippocampus but were most prominent in CA1. These gyrifications were also echoed in the underlying DG (where the term dentation is often used to refer to this feature), and region CA4 that the DG partially encircles. Each of these

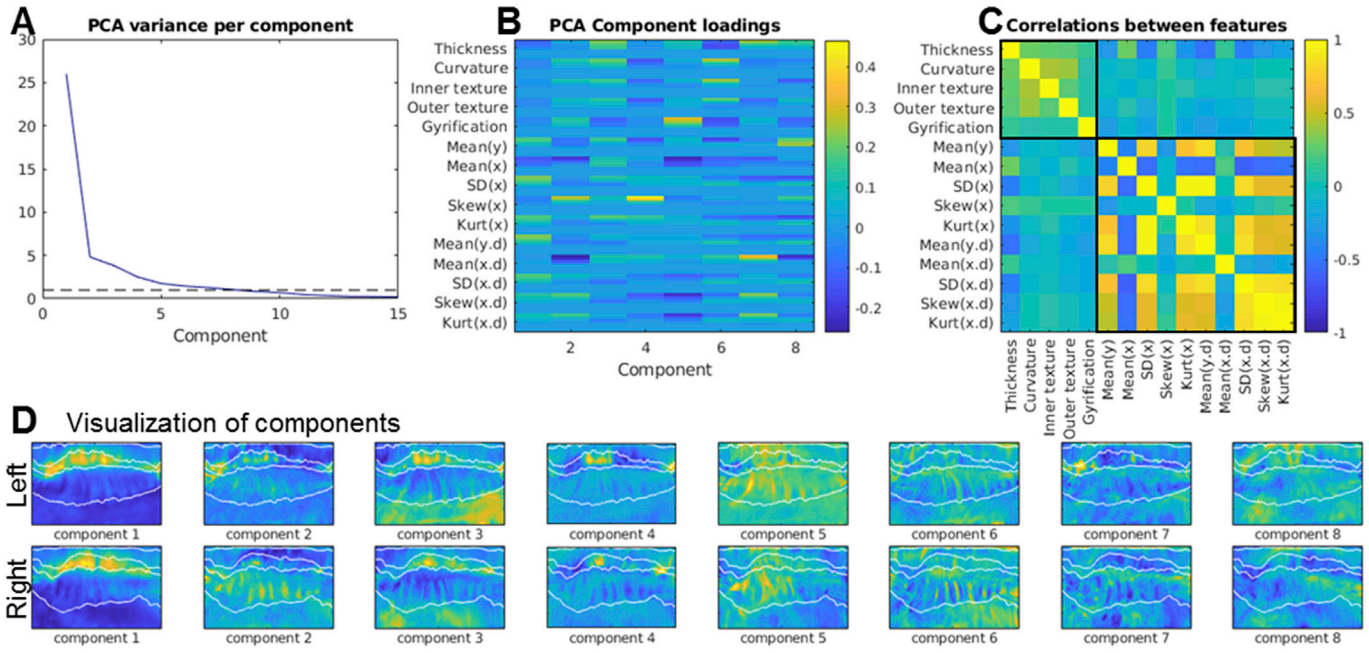

Fig. 5. Exploration of inherent feature variance. A) shows PCA component loadings from each feature with a dotted line at 1% after which subsequent components were discarded. B) shows the feature loadings of the first 8 components, with multiple rows for the various smoothing kernels applied to each feature. C) shows the correlation between all features, with separate boxes around morphological and laminar features. D) shows a visualization of the first 8 components, with manually defined subfield borders overlaid in white.

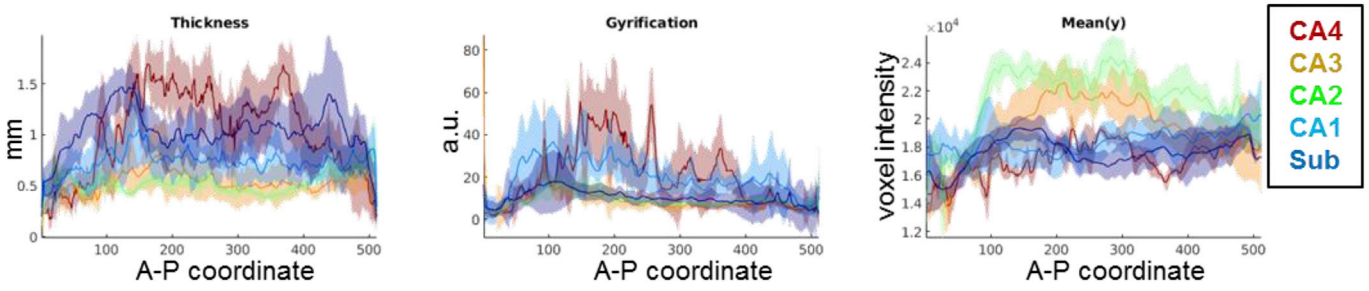

Fig. 6. Features of interest plotted with respect to the anterior-posterior axis of the hippocampus. Colours indicate manually defined subfields, and shaded areas indicate standard deviation. Data are combined across the left and right hippocampi. a.u. stands for arbitrary units, see Materials and Methods section for additional details.

Table 2
Dice overlap scores between k-means clusters and their closest corresponding manually defined subfield.

	All features		Laminar features		Morphological features	
	Left	Right	Left	Right	Left	Right
Sub	0.87	0.83	0.83	0.79	0.92	0.87
CA1	0.67	0.63	0.61	0.61	0.80	0.74
CA2	0.72	0.67	0.73	0.68	0	0
CA3	0.56	0.55	0.53	0.52	0.59	0.56
CA2&CA3	0.84	0.77	0.84	0.75	0.84	0.80
CA4	0.59[a]	0.41[a]	0	0	0	0

[a] After additional post-processing (see text).

features has been described in histology (Duvernoy et al., 2013; Ding and Van Hoesen, 2015), but has not been reconstructed in a 3D model at this level of detail. For example (Adler et al., 2018), and (Iglesias et al., 2015) both performed detailed and fully 3D segmentation of the hippocampus and its subfields using ex-vivo MRI data, with additional histological data in the same participants provided by Adler et al. Our approach extends these studies by utilizing higher-resolution tracing and by using histological cues inherent in the same images. Furthermore, our manual traces and quantitative analyses fully respect the topology of the hippocampus and, in turn, the continuity of each subfield throughout the entire length of the hippocampus. We note that the topology developed here does not cover the dentate gyrus, which has its own topological arrangement that is perpendicular to the rest of the cortex (including archi- and neo-cortex). This difference in topology arises from a different trajectory in ontogeny, in which the DG 'breaks with' the rest of the cortex and wraps around the distal-most archicortex, i.e., CA4 (Duvernoy et al., 2013; Nieuwenhuys et al., 2013). In future work, the DG could also be unfolded using a general framework similar to what is presented here. Critically, however, this approach would require employment of endpoints in a different plane.

After applying our topological unfolding framework, we computationally extracted morphological and laminar features from the hippocampus (Fig. 3). Many of these features agree with qualitative descriptions by neuroanatomists, as discussed in the Results section. Some of these features may be informative for in-vivo imaging as well. For example, measures of thickness and gyrification can be obtained under our topological unfolding framework given sufficiently detailed segmentations, regardless of the availability of cytoarchitectonic

features. These two features in particular show good contrast between subfields subiculum, CA1, and CA4. Thus, they could be explicitly leveraged to guide segmentation or registration to histological reference materials in future MRI work. This may have been underappreciated in other in-vivo studies, including our own previous MRI study, where some of the gyrifications in the body and tail of the hippocampus could not be detected. This prior lack of detail would also lead to overinflated thickness measures, larger overall volumes, and perhaps differences in the proportional sizes of some subfields along the anterior-posterior extent of the hippocampus. Quantitative MR, such as T1 mapping, may additionally provide cues to approximate cytoarchitectonic features. Indeed, in our previous work we observed higher T1-weights in CA2 and CA3 (DeKraker et al., 2018), which may be driven by the higher neuronal cell densities observed in the current study. Thus the features described here show clear promise for characterising or segmenting the hippocampus in future MRI work.

4.2. Unsupervised clustering of all features reveals hippocampal subfields

We performed unsupervised clustering of all features to determine whether we could identify the classically described hippocampal subfields using a completely unsupervised computational approach. Results from clustering yielded generally high overlap with manual subfield segmentations in most cases (Table 2), with several exceptions that are outlined in the Results section. One particularly interesting observation was that CA4 was consistently assigned the same cluster as CA3 or CA1, even though it shares no topological boundary with CA1. The shared structural elements between CA4 and CA1, particularly their relatively high thickness, gyrification, and low density of neurons, may relate to why certain diseases, such as subtypes of epilepsy, selectively affect CA1 and CA4 similarly (Duvernoy et al., 2013; Blümcke et al., 2013). In future imaging work, CA1 and CA4 may be differentiated from each other, particularly under our unfolding framework, due to their topological separation.

Finally, to further explore the inherent dimensionality of the structural feature space under consideration, we also examined its principle components (Fig. 5). In these analyses, we noted that the most prominent components varied in ways that followed the contours of some or all subfield borders (see Results section). This pattern suggests that the inherent structural variance in the hippocampus most naturally follows a proximal-distal patterning, as seen in the classic histological subfield definitions. Some components additionally hinted at inherent anterior-posterior differences across the hippocampus.

4.3. Morphological features are sufficient to approximate most subfield boundaries

In addition to clustering using all features, we also asked whether hippocampal subfields could be derived using only the subset of morphological features or the subset of laminar features (Fig. 4 and Table 2). Clustering using laminar features revealed all hippocampal subfields with reasonable accuracy with respect to manually defined gold standard segmentations (except CA4, and CA2 versus CA3 were not easily distinguished from one another). This was expected, since laminar features provide the key criteria used by histologists to define subfield boundaries (e.g. Duvernoy et al., 2013; Ding and Van Hoesen, 2015). However, when we examined morphological features alone we also found unsupervised clusters that closely resembled subfields subiculum, CA1, and a combined CA2 and CA3 region. Additionally, CA4 was assigned the same clusters as CA1, similar to when clustering was performed on all features combined. This outcome was not expected based on histological data, and provides support for the notion that morphological features capture an independent set of subfield-related structural elements. The observation that morphological feature are sufficient to determine most subfield boundaries holds great promise for future refinement of MRI protocols for subfield delineation, given that histological- or laminar-level details are not available in current imaging protocols. Indeed, many of the MR-based subfield segmentation protocols presently available rely on some combination of structural landmarks within or surrounding the hippocampus, but only indirectly on morphological features (see Yushkevich et al., 2015a).

4.4. Anterior-posterior structural variation

Anterior-posterior structural differences in the hippocampus are particularly of interest, given the growing body of literature suggesting functional gradients along the longitudinal axis of the hippocampus (e.g. Strange et al., 2014; Poppenk et al., 2013; Plachti et al., 2019; Zeidman and Maguire, 2016). Structural anterior-posterior gradients are difficult to assess using conventional histology, given that coronal or sagittal sections are typically out of plane with respect to the different subfields in most of the hippocampal head and tail. This highlights the utility of the 3D BigBrain dataset. Fig. 6 shows features gyrification, thickness, and neuronal density along the anterior-posterior axis of the hippocampus. Most notable anterior-posterior differences included differences in most features at the very anterior and posterior extents of the hippocampus. Previous work by (Ding and Van Hoesen, 2015) described the anterior most region - the vertical component of the uncus - as containing modified subfields that were much thinner than their counterparts throughout the rest of the hippocampus, consistent with our observations.

Gyrificaton was low in the anterior uncus, high in the remainder of the hippocampal head, and gradually decreased towards the posterior end of the hippocampus, most notably in CA1. Qualitatively, similar trends in gyrification have been observed in our previous 7T MRI study (DeKraker et al., 2018) and in other work (Chang et al., 2018). However, both of these studies were limited in their ability to detect small gyrifications (i.e. those detected in this study had peak-to-peak distances as low as 2 mm). Biophysical models of the development of gyrification suggest a relationship between gyrus size and cortical thickness (Zilles et al., 2013; Striedter et al., 2015). Yet, no systematic anterior-posterior differences in thickness were seen in the present data despite clear decreases in gyrification size towards the posterior extent. Other structures such as white matter might also constrain gyrification patterns (Striedter et al., 2015), which may additionally have consequences for functional properties of different gyri. For example (Henderson and Robinson, 2014), examined gyrification and structural connectivity in the neocortex and found more unified or modular graph theoretical properties within gyri, as opposed to sulcal regions which were more diffusely connected or hub-like. Similarly (Plachti et al., 2019; Libby et al., 2012), recently performed parcellation of the hippocampus according to its functional connectivity and observed divisions primarily along the anterior-posterior extent of the hippocampus, rather than across subfields (although some proximal-distal clustering was also observed, as in the present study). This functional parcellation may even relate to modular divisions of function within a given gyrus, as proposed for the neocortex by (Henderson and Robinson, 2014).

It is also interesting that neuronal density increased from anterior to posterior sections in subfields CA1 and CA4 in the present study. It should be noted that the current methods cannot differentiate density from neuronal size, but other related work has also found similar effects in density (Dam and Mouritzen Dam, 1979).

4.5. MRI applications and future directions

There are several clear implications of this work for in-vivo neuroimaging studies of the human hippocampus. Firstly, as described in the Introduction section, considerable research has gone into defining the hippocampal subfields according to available landmarks in MRI. Yet, relatively few studies have explicitly investigated the 3D shape of the underlying archicortex in which those subfields are embedded. Most subfield delineations rely directly or indirectly on manual segmentation

performed predominantly in the coronal view, in which the only visible gyrifications are in the hippocampal head (Yushkevich et al., 2015a). Because of this complication, many protocols have elected not to divide subfields in this region, or else to simplify them. The same concern also applies in the hippocampal tail, albeit at an even finer spatial scale. In our previous 7T MRI study (DeKraker et al., 2018), we demonstrated the use of topological modelling to overcome this challenge, but we note that this previous work captured fewer details than the current histological study due to resolution limitations. In future work, we anticipate it will be possible to explicitly model gyrifications and all other aspects of hippocampal topology considered in the present study. In addition, topological modelling of the hippocampus in MRI can open new lines of structural investigation, including the development of more precise measures of thickness, gyrification, and, at higher resolutions, potentially laminar features. Our approach promises to be of particular value in overcoming systematic partial voluming with white matter structures within the hippocampus and in adjacent structures. At a broader level, consideration of the hippocampal features highlighted in our study may also allow researchers and clinicians to link pathological changes, or behavioural and cognitive phenotypes, to more specific structural elements within the hippocampus. Finally, our current results may also help bridge the gap between microcircuit level modelling of the hippocampus and subfield modelling at the scales currently available in MRI. Because we found that subfields are characterized by unique morphological feature combinations, we may even be able to infer a relationship between subfield microcircuitry and fMRI measures in future work.

5. Data and resources made available

Alongside this publication, we release our detailed manually defined hippocampal subfields, unsupervised clustering results, topological unfolding framework, Equivolume laminar model solutions, and each of the unfolded morphological and laminar features computed here for the BigBrain dataset. These resources can be used as templates in other studies,. Alternatively, registration of these features to new data in our unfolded space can be used to guide future subfield segmentation. In addition, we have also made the code used in this project available via Open Science Framework (https://osf.io/x542s/). A toolbox for performing hippocampal unfolding, feature extraction, and other useful operations on more general datasets can be found at https://github.com/jordandekraker/Hippunfolding.

6. Conclusions

In the current project, we mapped the human hippocampus in detail by combining three methods. First, we used a unique dataset, BigBrain, that contains both histological-level detail and macroscopic 3D spatial context. Second, we imposed a topological unfolding framework to the hippocampus. Third, with this framework we extracted a set of morphological and laminar features, the latter of which have been used prolifically in neocortical characterization and parcellation. Using these methods we highlight three novel empirical observations. First, unsupervised clustering of these features closely resembles classically defined hippocampal subfields. Secondly, despite traditional reliance on laminar features in histology, morphological feature alone are sufficient to closely approximate most hippocampal subfields. Finally, some features such as gyrification in CA1 show, at least qualitatively, subfield-specific anterior-posterior differences that might relate to functional differences described in the extant literature. Overall, these findings highlight new structural characteristics of the hippocampus, and offer promising avenues for improved delineation and characterization of hippocampal subfields using in-vivo neuroimaging.

Acknowledgements

This work was supported by a Canadian Institutes for Health Research Project Grant (CIHR Grant # 366062) to A.K. and S.K.. J.D. was funded through a Natural Sciences and Engineering Research Council doctoral Canadian Graduate Scholarship (NSERC CGS-D). J.C.L was funded through the Western University Clinical Investigator Program accredited by the Royal College of Physicians and Surgeons of Canada and a Canadian Institutes of Health Research (CIHR) Frederick Banting and Charles Best Canada Graduate Scholarship Doctoral Award. K.M.F.- was funded through an Ontario Graduate Scholarship (OGS).

We would also like to thank Dr. Alan Evans, Dr. Katrin Amunts, and all contributors to BigBrain for developing and releasing this invaluable resource.

Appendix A. Supplementary data

Supplementary data to this article can be found online at https://doi.org/10.1016/j.neuroimage.2019.116328.

References

Adler, D.H., Wisse, L.E.M., Ittyerah, R., Pluta, J.B., Ding, S.-L., Xie, L., et al., 2018. Characterizing the human hippocampus in aging and Alzheimer's disease using a computational atlas derived from ex vivo MRI and histology. Proc. Natl. Acad. Sci. U. S. A. 115 (16), 4252–4257. Apr 17.

Amunts, K., Schleicher, A., Bürgel, U., Mohlberg, H., Uylings, H.B.M., Zilles, K., 1999. Broca's region revisited: cytoarchitecture and intersubject variability. J. Comp. Neurol. 412 (2), 319–341.

Amunts, K., Lepage, C., Borgeat, L., Mohlberg, H., Dickscheid, T.,-E., Rousseau, M., et al., 2013. BigBrain: an ultrahigh-resolution 3D human brain model. Science 340 (6139), 1472–1475.

Blümcke, I., Thom, M., Aronica, E., Armstrong, D.D., Bartolomei, F., Bernasconi, A., et al., 2013. International consensus classification of hippocampal sclerosis in temporal lobe epilepsy: a Task Force report from the ILAE Commission on Diagnostic Methods. Epilepsia 54 (7), 1315–1329. Jul.

Cai, S., Yu, X., Zhang, Q., Huang, C., Gao, Y., 2019. In: Is hippocampus Getting Bumpier with Age: a Quantitative Analysis of Fine-Scale Dentational Feature under the hippocampus on 552 Healthy Subjects [Internet]. Medical Imaging 2019: Image Processing. Available from:

Chang, C., Huang, C., Zhou, N., Li, S.X., Ver Hoef, L., Gao, Y., 2018. The bumps under the hippocampus. Hum. Brain Mapp. 39 (1), 472–490. Jan.

Dam, A.M., Mouritzen Dam, A., 1979. The density of neurons in the human Hippocampus [internet], 5. Neuropathology and Applied Neurobiology, pp. 249–264. Available from:

DeKraker, J., Ferko, K.M., Lau, J.C., Köhler, S., Khan, A.R., 2018. Unfolding the hippocampus: an intrinsic coordinate system for subfield segmentations and quantitative mapping. Neuroimage 167, 408–418. Feb 15.

Dice, L.R., 1945. Measures of the amount of ecologic association between species. Ecology 26 (3), 297–302.

Ding, S.-L., 2013. Comparative anatomy of the prosubiculum, subiculum, presubiculum, postsubiculum, and parasubiculum in human, monkey, and rodent. J. Comp. Neurol. 521 (18), 4145–4162. Dec 15.

Ding, S.-L., Van Hoesen, G.W., 2015. Organization and detailed parcellation of human hippocampal head and body regions based on a combined analysis of cyto- and chemoarchitecture. J. Comp. Neurol. 523 (15), 2233–2253. Oct 15.

Duvernoy, H.M., Cattin, F., Risold, P.-Y., 2013. The Human Hippocampus.

Henderson, J.A., Robinson, P.A., 2014. Relations between the geometry of cortical gyrification and white-matter network architecture. Brain Connect. 4 (2), 112–130. Mar.

Iglesias, J.E., Augustinack, J.C., Nguyen, K., Player, C.M., Player, A., Wright, M., et al., 2015. A computational atlas of the hippocampal formation using ex vivo, ultra-high resolution MRI: application to adaptive segmentation of in vivo MRI. Neuroimage 115, 117–137. Jul 15.

Landman, B.A., Bogovic, J.A., Carass, A., Chen, M., Roy, S., Shiee, N., et al., 2013. System for integrated neuroimaging analysis and processing of structure. Neuroinformatics 11 (1), 91–103. Jan.

Larsen, R., Nielsen, M., Sporring, J., 2006. In: Medical Image Computing and Computer-Assisted Intervention – MICCAI 2006: 9th International Conference, Copenhagen, Denmark, October 1-6, 2006, Proceedings. Springer Science & Business Media, p. 981.

Libby, L.A., Ekstrom, A.D., Ragland, J.D., Ranganath, C., 2012. Differential connectivity of perirhinal and parahippocampal cortices within human hippocampal subregions revealed by high-resolution functional imaging. J. Neurosci. 32 (19), 6550–6560. May 9.

Nieuwenhuys, R., Voogd, J., van Huijzen, C., 2013. The Human Central Nervous System: A Synopsis and Atlas. Springer Science & Business Media, p. 256.

Plachti, A., Eickhoff, S.B., Hoffstaedter, F., Patil, K.R., Laird, A.R., Fox, P.T., et al., 2019. Multimodal parcellations and extensive behavioral profiling tackling the Hippocampus gradient [Internet] Cereb. Cortex. https://doi.org/10.1093/cercor/bhy336. Feb 4; Available from:

Poppenk, J., Evensmoen, H.R., Moscovitch, M., Nadel, L., 2013. Long-axis specialization of the human hippocampus. Trends Cogn. Sci. 17 (5), 230–240. May.

Schleicher, A., Amunts, K., Geyer, S., Morosan, P., Zilles, K., 1999. Observer-independent method for microstructural parcellation of cerebral cortex: a quantitative approach to cytoarchitectonics. Neuroimage 9 (1), 165–177. Jan.

Small, S.A., Schobel, S.A., Buxton, R.B., Witter, M.P., Barnes, C.A., 2011. A pathophysiological framework of hippocampal dysfunction in ageing and disease. Nat. Rev. Neurosci. 12 (10), 585–601. Sep 7.

Sørensen, T., 1948. A Method of Establishing Groups of Equal Amplitude in Plant Sociology Based on Similarity of Species Content and its Application to Analyses of the Vegetation on Danish Commons, p. 34.

Strange, B.A., Witter, M.P., Lein, E.S., Moser, E.I., 2014. Functional organization of the hippocampal longitudinal axis. Nat. Rev. Neurosci. 15 (10), 655–669. Oct.

Striedter, G.F., Srinivasan, S., Monuki, E.S., 2015. Cortical folding: when, where, how, and why? Annu. Rev. Neurosci. 38, 291–307. Jul 8.

Waehnert, M.D., Dinse, J., Weiss, M., Streicher, M.N., Waehnert, P., Geyer, S., et al., 2014. Anatomically motivated modeling of cortical laminae. Neuroimage 93, 210–220.

Wagstyl K, Larocque S, Cucurull G, Lepage C, Cohen JP, Bludau S, et al. Automated segmentation of cortical layers in BigBrain reveals divergent cortical and laminar thickness gradients in sensory and motor cortices [Internet]. Available from: https://doi.org/10.1101/580597.

Wagstyl, K., Lepage, C., Bludau, S., Zilles, K., Fletcher, P.C., Amunts, K., et al., 2018. Mapping cortical laminar structure in the 3D BigBrain. Cerebr. Cortex 28 (7), 2551–2562. Jul 1.

Wisse, L.E.M., Daugherty, A.M., Olsen, R.K., Berron, D., Carr, V.A., Stark, C.E.L., et al., 2017. A harmonized segmentation protocol for hippocampal and parahippocampal subregions: why do we need one and what are the key goals? Hippocampus 27 (1), 3–11. Jan.

Yushkevich, P.A., Piven, J., Hazlett, H.C., Smith, R.G., Ho, S., Gee, J.C., et al., 2006. User-guided 3D active contour segmentation of anatomical structures: significantly improved efficiency and reliability. Neuroimage 31 (3), 1116–1128. Jul 1.

Yushkevich, P.A., Avants, B.B., Pluta, J., Das, S., Minkoff, D., Mechanic-Hamilton, D., et al., 2009. A high-resolution computational atlas of the human hippocampus from postmortem magnetic resonance imaging at 9.4 T. Neuroimage 44 (2), 385–398. Jan 15.

Yushkevich, P.A., Amaral, R.S.C., Augustinack, J.C., Bender, A.R., Bernstein, J.D., Boccardi, M., et al., 2015. Quantitative comparison of 21 protocols for labeling hippocampal subfields and parahippocampal subregions in in vivo MRI: towards a harmonized segmentation protocol. Neuroimage 111, 526–541. May 1.

Yushkevich, P.A., Pluta, J.B., Wang, H., Xie, L., Ding, S.-L., Gertje, E.C., et al., 2015. Automated volumetry and regional thickness analysis of hippocampal subfields and medial temporal cortical structures in mild cognitive impairment. Hum. Brain Mapp. 36 (1), 258–287. Jan.

Zeidman, P., Maguire, E.A., 2016. Anterior hippocampus: the anatomy of perception, imagination and episodic memory. Nat. Rev. Neurosci. 17 (3), 173–182. Mar.

Zilles, K., Palomero-Gallagher, N., Amunts, K., 2013. Development of cortical folding during evolution and ontogeny. Trends Neurosci. 36 (5), 275–284. May.